https://doi.org/10.5194/tc-2020-269
Preprint. Discussion started: 7 October 2020

The Cryosphere Discussions Open Access EGU

The retrieval of snow properties from SLSTR/ Sentinel-3 - part 1: method description and sensitivity study

Linlu Mei[1], Vladimir Rozanov[1], Christine Pohl[1], Marco Vountas[1], John P. Burrows[1]

[1] Institute of Environmental Physics, University of Bremen, Germany

Abstract

The eXtensible Bremen Aerosol/cloud and surfacE parameters Retrieval (XBAER) algorithm has been applied on the Top-Of-Atmosphere reflectance measured by the Sea and Land Surface Temperature Radiometer (SLSTR) instrument onboard Sentinel-3 to derive snow properties: Snow Grain Size (SGS), Snow Particle Shape (SPS) and Specific Surface Area (SSA) under cloud-free conditions. This is the first part of the paper, to describe the retrieval method and the sensitivity study. Nine pre-defined ice crystal particle shapes (aggregate of 8 columns, Drontal, hollow bullet rosettes, hollow column, plate, aggregate of 5 plates, aggregate of 10 plates, solid bullet rosettes, column) are used to describe the snow optical properties. The optimal SGS and SPS are estimated iteratively utilizing a Look-Up-Table (LUT) approach. The SSA is then calculated using another pre-calculated LUT for the retrieved SGS and SPS. The optical properties (e.g., phase function) of the ice crystals can reproduce the wavelength-dependent/angular-dependent snow reflectance features, compared to laboratory measurements. A comprehensive study to understand the impact of aerosol, ice crystal shape, ice crystal surface roughness, and cloud contamination on the retrieval accuracy of snow properties has been performed based on SCIATRAN radiative transfer simulations. The main findings are (1) Snow angular and spectral reflectance feature can be described by the predefined ice crystal properties only when both SGS and SPS can be optimally and iteratively obtained; (2) The impact of ice crystal surface roughness plays minor effects on the retrieval results; (3) SGS and SSA show an inverse linear relationship; (4) The retrieval of SSA assuming non-convex particle shape, compared to convex particle (e.g. sphere) shows larger results; (5) Aerosol/cloud contamination

https://doi.org/10.5194/tc-2020-269
Preprint. Discussion started: 7 October 2020

The Cryosphere Discussions

due to unperfected atmospheric correction and cloud screening introduces underestimation of SGS, "inaccurate" SPS and overestimation of SSA.

1 Introduction

Snow properties such as snow albedo, Snow Grain Size (SGS), Snow Particle Shape (SPS), Specific Surface Area (SSA), snow purity (Warren and Wiscombe, 1980; Painter et al., 2003; Hansen and Nazarenko, 2004; Taillandier et al., 2007; Gallet et al., 2009; Battaglia et al., 2010; Gardner et al., 2010; Domine et al., 2011; Liu et al., 2012; Qu et al., 2015; Baker et al., 2019; Pohl et al., 2020a) show large variabilities temporally and spatially (Kukla et al., 1986). They play important roles in the global radiation budget, which is critical to some well-known phenomenon such as the Arctic amplification (Serreze and Francis, 2006; Domine et al., 2019). Satellites offer an effective way to understand the surface-atmosphere processes and corresponding feedback mechanisms on the regional, continental and/or global scales (Konig et al., 2001; Pope et al., 2014). Satellite derived snow products (e.g., SGS, SPS, and SSA) are particularly important for short-term hydrological, meteorological and climatological modelling (Livneh et al., 2009). A high-quanlity snow property data product can also be applied to derive Aerosol Optical Thickness (AOT) over cryosphere (Mei et al., 2020a). High-quality satellite derived snow products and their by-products are also important for the creation of long-term "Climate Data Records" (SSMC, 2014), which enable a better investigation and interpretation concerning global climate change (Konig et al., 2001).

A comprehensive overview of remote sensing of SGS, SPS, and SSA can be found in many previous publications (e.g., Li et al., 2001; Stamnes et al., 2007; Koren, 2009; Lyapustin et al., 2009; Dietz et al., 2012; Wiebe et al., 2013; Frei et al., 2012; Mary et al., 2013; Kokhanovsky, et al., 2019; Xiong et al., 2018). The variation of SGS leads to the large variability of Top Of Atmosphere (TOA) reflectance in NIR/SWIR spectral ranges while SPS shows a strong impact on TOA reflectance at visible channels (Warren and Wiscombe, 1980). Different retrieval algorithms have been developed for different instruments. For instance, the MODIS Snow Covered-Area and Grain size (MODSCAG) retrieval algorithm and Multi-Angle

https://doi.org/10.5194/tc-2020-269
Preprint. Discussion started: 7 October 2020

The Cryosphere Discussions

Implementation of Atmospheric Correction (MAIAC) algorithm have been used to derive SGS using MODIS and VIIRS instruments (Painter et al., 2003; 2009; Lyapustin et al., 2009).

Snow particle shape is another important parameter which affects the estimation of snow properties, such as albedo (Räisänen et al., 2017; Flanner and Zender, 2006), because ice crystals with different shapes have different optical properties (Jin et al., 2008; Yang et al., 2013). The absorption and extinction cross-sections of an ice crystal can be described as a function of size, shape, and refractive index at a given wavelength (van de Hulst 1981; Mischenko et al., 2002 and references therein). Natural snow consists of grains, depending on temperature, humidity, and meteorological conditions, which have numerous different shapes (Nakaya, 1954). Ice crystal shapes have been classified into different categories, the classification has been increased from 21 (Nakaya and Sekido, 1938) to 121 categories (Kikuchi et al., 2013). Although spherical shape assumption is typically used for field measurements (Flanner and Zender, 2006; Donahue et al., 2020), this approximation is not recommended to be used in retrieval algorithms of satellite measurements because it leads to large differences between observed and simulated wavelength-dependent snow bidirectional reflectance, especially at visible wavelengths (Leroux and Fily et al., 1998; Aoki et al., 2000; Jin et al., 2008; Dumont et al., 2010; Libois et al., 2013). Improper wavelength-dependent snow bidirectional reflectance caused by a predefined ice crystal shape leads to low-quality satellite retrieval results. Some attempts to derive ice crystal shape in the ice cloud can be found in previous publications (McFarlane et al., 2005; Cole et al., 2014).

According to Legagneux et al., (2002), SSA is defined as the surface area of ice crsytal per unit mass, i.e., SSA = $A_t/\rho V$, where A_t and V are total surface area and volume, respectively, ρ is the ice density. SSA includes information on both SGS and SPS and it is often used to describe the surface area available for chemical processes (Taillandier et al., 2007; Domine et al., 2011; Yamaguchi et al., 2019). SSA is reported to have a good relationship with snow spectral albedo at the short wave infrared wavelengths (Domine et al., 2007). Optical methods are routinely used to measure SSA in the field (Gallet et al., 2009). Empirical equations have been proposed to describe the change of SSA (Legagneux and Domine, 2005; Taillandier et al.,

https://doi.org/10.5194/tc-2020-269
Preprint. Discussion started: 7 October 2020

The Cryosphere Discussions

2007). Few attempts have been made to derive SSA from satellite observations (Mary et al., 2013; Xiong et al., 2018).

This paper presents a new retrieval algorithm to derive SGS, SPS, and SSA from satellite observations. In a snow-atmosphere system, satellite observed TOA reflectances are affected by numerous snow and atmospheric parameters. The parameters, which will be estimated in the framework of the eXtensible Bremen Aerosol/cloud and surfacE parameters Retrieval (XBAER) algorithm, will be called the target parameters. Other parameters, which the TOA reflectance also depends on, will be called the model parameters. In the case of the XBAER algorithm, the target parameters are SGS, SPS, and SSA, whereas the model parameters are aerosol loading, cloud optical thickness, and gaseous absorption. Throughout the paper, SGS will be characterized by an effective radius. Following Baum et al., (2011), the effective radius is defined as $3V/(4A_p)$, where V and A_p are the volume and average projected area, respectively. As can be seen, in the case of a spherical particle, the effective radius is equal to the radius of the sphere. The general concept of the retrieval algorithm is to use simultaneously spectral and angular reflectance measurements, which are sensitive to SGS and SPS. The spectral channels used in the XBAER algorithm are 0.55 μm and 1.6 μm. Both nadir and oblique observation directions from SLSTR are used. An optimal SGS and SPS pair is achieved by minimizing the difference between measured and simulated atmospheric-corrected surface reflectances. SSA is then calculated based on the retrieved SGS and SPS. Nine predefined ice crystal particle shapes (aggregate of 8 columns, droxtal, hollow bullet rosettes, hollow column, plate, aggregate of 5 plates, aggregate of 10 plates, solid bullet rosettes, column) (Yang et al., 2013, see Table 1) are used to describe the snow optical properties and to simulate the snow surface reflectance at 0.55 and 1.6 μm at two observation angles.

Three points we would like to emphasize to avoid misunderstandings between snow science community and remote sesning community.

- **Usage the Yang et al (2013) database for ice crystal in the air (ice cloud) and on the ground (snow).** The optical properties of ice crystals presented by Yang et al., (2013) have been widely used to study ice clouds. In recent publications, it has been

https://doi.org/10.5194/tc-2020-269
Preprint. Discussion started: 7 October 2020

demonstrated that they can also be used for snow studies (Räisänen et al, 2015; Pirazzini et al., 2015; Saito et al., 2019; Schneider et al., 2019; Pohl et al., 2020b). In fact, the single-scattering properties of ice crystals in Yang et al., (2013) database are determined solely by given particle size, shape, and refractive index. They can be used to describe the optical properties of both snow particles and ice cloud particles when the particle models represent the aforementioned optical/physical properties (Saito et al., 2019; Personal communication with Dr. Saito).

- **Ice crystal shape observed from field measurements and derived from satellite observations**. For scientists working in a laboratory or on campaign-based studies, the best way to get an image of snow is to use an X-ray microtomography or confocal scanning optical microscope/scanning electron microscope (Hagenmuller et al., 2016; Baker et al., 2019; Personal communication with Dr. Ian Baker). In a field measurement and its related application areas (e.g., calculation of snow albedo), a spherical shape assumption is widely used because it is easier to derive other snow properties such as SSAs and snow albedo based on this assumption, compared to other more complicated shapes (see Appendix). The assumption of spherical and non-spherical shape has much less impact on the estimation of snow albedo compared to the bidirectional reflection features of snow (Grenfel and Warren, 1999; Dumont et al., 2010). Because SPS has a significant impact on the ice crystal phase function while it has a relatively weak impact on the snow extinction/absorption coefficient (Jin et al., 2008). However, the spherical shape cannot be used to provide typical bidirectional reflection features of snow with required accuracy (Jin et al., 2008; Dumon et al., 2010; Jiao et al., 2019), which is the fundamental basis to derive snow properties from satellite remote sensing techniques. Thus, more complicated ice crystal shapes, such as those proposed by Yang et al (2013), are recommended to use in the simulations of the angular distribution of snow reflectance;

- **SGS and SSA**. Although the definition of snow grain constitutes is an ongoing debate in different communities, SGS and SPS are two fundamental inputs for any radiative transfer model, which is the basis for the satellite retrievals (Langlois et al., 2020).

https://doi.org/10.5194/tc-2020-269
Preprint. Discussion started: 7 October 2020

The Cryosphere Discussions
Open Access

Typically, the SSA is more preferable within the snow science community because SSA is commonly used in further applications based on field measurements. We note, however, according to the definition of SSA, for a given SPS, a unique relationship between SGS and SSA can be derived.

This paper is structured as follows: observations characteristics of SLSTR and the laboratory measurements used for sensitivity studies are described in section 2. The theoretical background and the ice crystal database (Yang et al., 2013) are presented in section 3. Section 4 describes the eXtensible Bremen Aerosol/cloud and surfacE parameters Retrieval (XBAER) algorithm. The results of a comprehensive sensitivity study using SCIATRAN (Rozanov et al., 2014) simulations are presented in section 5. The conclusions are given in section 6.

Table 1 Snow grain type (shape) provided in Yang et al (2013) database. The abbreviations are introduced here will be used later

Grain Type	Abbreviation	Schematic drawing
Aggregate of 8 columns	col8e	
Droxtal	droxa	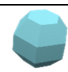
Hollow bullet rosettes	holbr	
Hollow column	holco	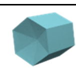
Plate	pla_1	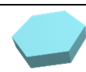
Aggregate of 5 plates	pla_5	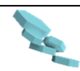
Aggregate of 10 plates	pla_10	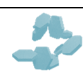
Solid bullet rosettes	solbr	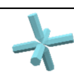

https://doi.org/10.5194/tc-2020-269
Preprint. Discussion started: 7 October 2020

The Cryosphere Discussions
Open Access
EGU

Column	solco	

2 Data

2.1 SLSTR instrument

The satellite data will be used twofold throughout the paper. In the first part, we perform a statistical analysis of the SLSTR observation/illumination geometries to select realistic settings for the sensitivity study. In the second part of the companion paper, the satellite measurements will be used as the inputs of the XBAER algorithm to derive the research satellite products of SGS, SPS, and SSA.

The SLSTR instrument onboard the European Space Agency (ESA) satellite Sentinel-3 is the successor of the Advanced Along-Track Scanning Radiometer (AATSR) instrument, which is used to maintain continuity with the (A)ATSR series of instruments. SLSTR takes the heritage of AATSR instrument characteristics, especially the dual-viewing observation capabilities and wavelength settings. In order to have a reasonable setting for observation/illumination geometries in the sensitivity study, we perform a statistical analysis of the SLSTR observation geometries (solar zenith angle, SZA, viewing zenith angle, VZA, relative azimuth angle, RAA), similar as Mei et al (2020a). This analysis is essential because 1) it provides a realistic setting of observation/illumination geometries in our sensitivity studies; 2) it helps us to have a complete understanding of the observation/illumination related surface/atmospheric properties. Here the definition of RAA has been harmonized with SCIATRAN (Rozanov et al., 2014), namely, RAA value is equal to 0° under strict glint condition. The statistical analysis has been performed using observations over Greenland during April and September 2017. April and September are reported to be representativeness months of the Arctic (Mei et al., 2020a). Fig. 1 shows the frequency of SLSTR observation geometries. The upper panel shows the SZA with SLSTR nadir and oblique observations for April and September. We can see that the SZA occurs frequently with a value of 70° for selected months. The VZA and RAA for oblique observation mode are typically around 55°

https://doi.org/10.5194/tc-2020-269
Preprint. Discussion started: 7 October 2020

The Cryosphere Discussions
Open Access
EGU

and in a range of [110°, 170°], respectively. The observation geometries for nadir observation show relatively large variabilities due to larger swath width compared to oblique (1400 km vs 700 km). Larger SZA can be found especially at the edge of the swath. The VZA and RAA for oblique observation mode are typically in ranges of [0°, 55°] and [70°, 140°], respectively. According to the statistical analysis, a combination of SZA, VZA, RAA of 70°, 30°, 135° for nadir observation and 70°, 55°, 135° for oblique observation can be a reasonable setting for the SLSTR observation geometries for the sensitivity study.

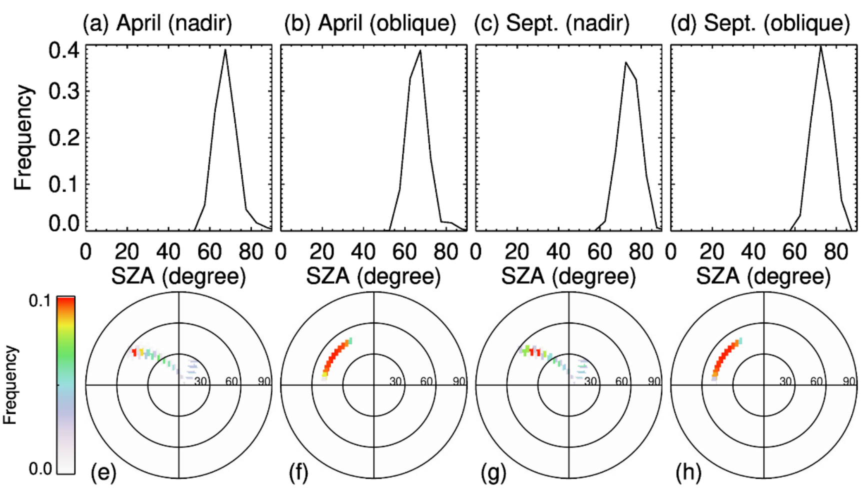

Fig. 1 Upper panel is the histograms of SZA for SLSTR observations: (a) nadir during April; (b) oblique during April, (c) nadir during September; (d) oblique during September. Lower panel is the polar plots of (VZA, RAA) probability for AATSR observations: (e) nadir during April; (f) oblique during April, (g) nadir during September; (h) oblique during September.

2.2 Laboratory measurements

Laboratory measurements of the bidirectional reflectance of snow samples contain important information about the dependence of the angular structure of snow reflection on the lighting geometry, wavelength, and snow physical properties. The comparison of measured and modeled bidirectional reflectance helps to establish the conceptual ideas for the retrieval

https://doi.org/10.5194/tc-2020-269
Preprint. Discussion started: 7 October 2020

The Cryosphere Discussions Open Access EGU

algorithm. For this comparison, we have selected measurements of fresh and aged snow samples presented by Dumont et al., (2010) and Peltoniemi et al., (2009), respectively.

The fresh snow sample, a cylinder of 30 cm diameter and 12 cm height, was taken from new wet snow layer at Col de Porte (Chartreuse, France) at 1300 meter above sea level during January 2008 (Dumont et al., 2010). The sample was stored in a cold room at -10°C for one week to avoid metamorphic effects during the ensuing measurements. To obtain the Bidirectional Reflectance Factor (BRF), the snow sample was illuminated by a monochromatic light source at incidence zenith angle of 60°. The spectral BRF between 500 and 2600 nm was measured at viewing zenith angles of 0°, 30°, 60°, 70° and relative azimuth angles 0°, 45°, 90°, 135°, 180° by a spectrogonio-radiometer developed at the Laboratoire de Planétologie de Grenoble, France, and using a Spectralon® and an infragold® sample as a reference (see Dumont et al., (2010) for further details).

The aged snow sample, a cuboid of more than 10 cm height, was taken from an old dry snow layer at Masala, Finland, and brought into a warm laboratory. The spectral BRF between 350 and 2500 nm was measured during the aged process by the Finnish geodetic institute field goniospectro-polariphotometer (FIGIFIGO) and using a Labsphere Spectralon 99% white reference plate. For illumination, a 1000 W Oriel Research Quartz tungsten halogen lamp at a zenith angle of 60° was utilized (Peltoniemi et al., 2009). Spectral BRF was obtained at viewing zenith angles up to 70° in 1° resolution and at relative azimuth angles of 0°, 90°, 130°, 160°, 180°, 270°, 310°, and 340°. The first and last measurements were done in the principal plane, indicating minor metamorphism in the snow layer during the measurement.

3 Dependence of snow reflectance on target parameters

A comprehensive data library (Yang et al., 2013) containing the scattering, absorption, and polarization properties of ice particles in the spectral range from 0.2 to 15 μm was used to calculate radiative transfer through a snow layer (Pohl et al., 2020b). A full set of single-scattering properties is available for nine ice crystal habits presented in Table 1. The maximum dimension of each habit ranges from 2 to 10000 μm in 189 discrete sizes.

The optical properties of ice crystals depend on wavelength, ice crystal size, and shape. Maximal dependence of the single-scattering albedo on the particle size is observed in the spectral ranges where ice absorption cannot be neglected. The asymmetry factor depends on the particle size for the whole spectral range. This dependence can be weaker or stronger at a selected wavelength depending on SPS (see Yang et al., (2013) for details).

To better illustrate the impact of SGS and SPS on the radiative transfer through a snow layer, we have calculated the reflectance of the snow layer consisting of droxtals, aggregates of 8 columns, hollow columns, and plates with crystal surface roughness condition as severely roughened. The simulations of snow reflectance were performed using the radiative transfer package SCIATRAN (Rozanov et al., 2014). The snow layer was defined as a layer directly over a black surface, with snow optical thickness of 500 and a snow geometrical thickness of 1m. The snow layer is assumed to be vertically and horizontally homogeneous without any surface roughness and composed of monodisperse ice crystals. The impact of snow impurities and scattering/absorption processes in the atmosphere was neglected at this stage. The reflectance of the snow layer as a function of the effective radius of ice crystal at wavelengths 0.55 μm and 1.6 μm is presented in Fig. 2. The calculations were performed for typical SLSTR instrument observation/illumination geometries (see section 2.1), with SZA, VZA, and RAA equal to 70°, 30°, and 135° (scattering angle 129°).

The right panel of Fig. 2 demonstrates the strong dependence of the snow layer reflectance at 1.6 μm on the SGS. One can also see that the dependence of snow reflectance on SPS cannot be neglected. In particular, the same reflectance can be obtained with a combination of different SGS and SPS. For instance, one can see from the right panel of Fig. 2 that, the reflectance of the snow layer consisting of droxtals with SGS=200 μm or of plates with SGS=65 μm equals ~0.035 in both cases. Thus, assuming different SPSs, the values of retrieved SGS can differ 3 times.

The left panel of Fig. 2 demonstrates the dependence of the snow layer reflectance at 0.55 μm on SGS and SPS. It can be seen that the dependence of reflectance on SGS is very weak for droxtals and aggregate of 8 columns. However, reflectance at 0.55 μm decreases with an

https://doi.org/10.5194/tc-2020-269
Preprint. Discussion started: 7 October 2020

increase of SGS for hollow columns and plates. The weak oscillations for the reflectances at 0.55 μm can be explained by the joint impact of oscillations in the single-scattering albedo and elements of the scattering matrix presented in the original database.

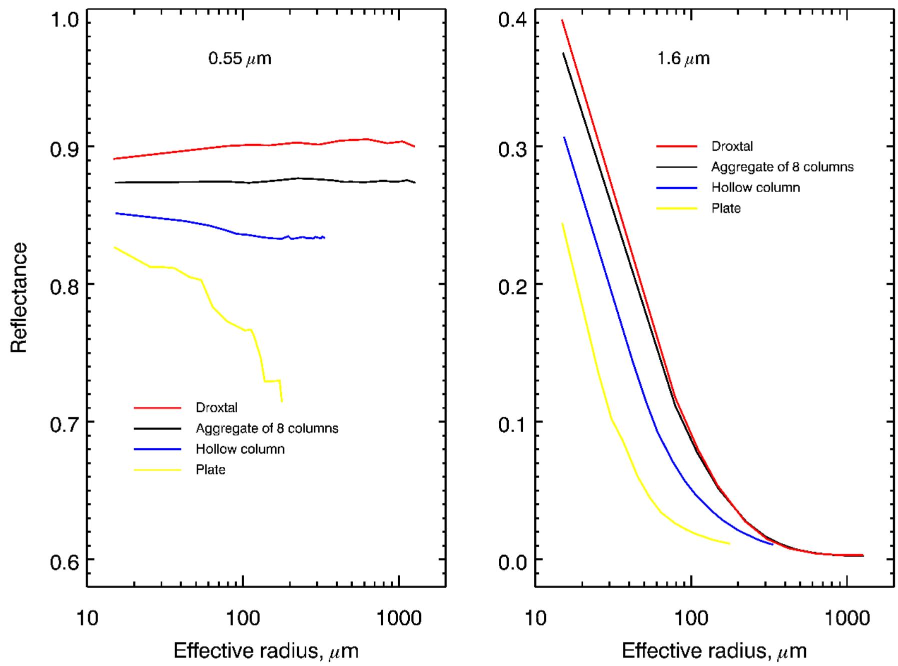

Fig 2. Reflectance of snow layer at 0.55 μm and 1.6 μm calculated assuming different SPS. Observation/illumination geometry: SZA, VZA and RAA were set to 70°, 30° and 135°, respectively.

To illustrate this point, the dependence of the phase function at 129° scattering angle on SGS is shown in the left panel of Fig. 3. The phase functions (F11 element of the scattering matrix) were extracted from the original database. According to the left panel of Fig. 3, the dependence of snow surface reflectance at 0.55 μm on SGS and SPS is caused mainly by the phase function of ice crystal. Weak oscillations can also be found.

The above analysis shows that accurate retrieval of SGS requires adequate information about SPS and accounting for the dependence of the phase function on SGS. To better illustrate the impacts of SGS on ice crystal phase function, we calculated reflectance at 1.6 μm with

https://doi.org/10.5194/tc-2020-269
Preprint. Discussion started: 7 October 2020

The Cryosphere Discussions
Open Access
EGU

different SGS values. The right panel of Fig. 3 represents the reflectance of the snow layer, consisting of aggregates of 8 columns, calculated accounting for the dependence of the phase function on the effective radius (black line) and assuming constant phase function for three selected effective radii equal to 15, 150, and 1150 µm (red, green, and blue lines, respectively). It can be seen that the accurate simulation of snow reflection requires accounting for the dependence of phase function on SGS.

The main findings of presented investigations can be formulated as follows:

- reflectance of a snow layer depends on both SGS and SPS;
- accurate simulation of snow surface reflectance requires accounting for the dependence of phase function on SGS;
- spectral channels in the visible spectral range is more sensitive to SPS compared to SGS;
- spectral channels in the near infrared spectral range is more sensitive to SGS compared to SPS.

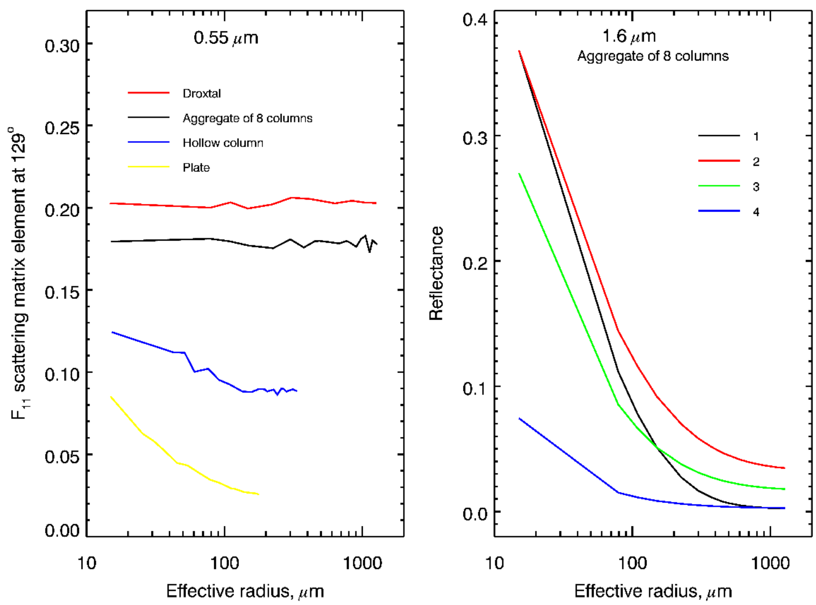

https://doi.org/10.5194/tc-2020-269
Preprint. Discussion started: 7 October 2020

The Cryosphere Discussions

Fig 3. Left panel: phase function at 0.55 μm for scattering angle of 129°, extracted from the original database (Yang et al., 2013) as a function of effective radius. Right panel: reflectance of snow layer at 1.6 μm consisting of aggregate of 8 columns, calculated assuming that: 1: phase function depends on the effective radius (black line); 2: phase function is constant corresponding to the effective radius 15μm (red line); 3: same as 2 but for effective radius of 150 μm (green line); 4: same as 2 but for effective radius of 1150 μm (blue line).

Although the global classification snow crystal, ice crystal, and solid precipitation particles suggested in Kikuchi et al. (2013) consist of the 121 particle types, we restrict ourselves, in the retrieval algorithm, with nine shapes of ice crystals, for which optical characteristics are represented in database (Yang et al., 2013). And these nine shapes have been proven to be used to reproduce typical wavelength/angular features of snow reflectance in reality, especially from satellite observations (Räisänen et al, 2015; Pirazzini et al., 2015; Saito et al., 2019; Schneider et al., 2019; Pohl et al., 2020b). To futher illustrate that the selected dataset is able to reproduce the BRF of different snow types, we compared the simulated and measured BRF of fresh (Dumont et al., 2010) and aged (Peltoniemi et al., 2009) snow samples. To reproduce the spectral BRF by SCIATRAN, we use the setup described above in this section and adjust the SGS for each SPS by minimizing the deviation between simulated and measured reflectance at 1.6 μm. Figure 4 shows the simulated BRF in the principal plane at 0.55 μm of fresh and aged snow samples, as well as the respective measurements. The BRF is defined as πI/F, where I is the reflected radiance and F is the incident irradiance. According to Fig. 4(a), for fresh snow, plates are the best shape to reproduce the measured BRF in the vicinity of the forward scattering peak but plates underestimate the BRF at higher viewing zenith angles in the backscattering region. Here, shapes of hollow bullet rosette, hollow column, aggregate of 10 plates exhibit better potential to simulate the fresh snow layer BRF. In the case of aged snow, shapes of solid and hollow column, hollow bullet rosette, and aggregate of 5 and 10 plates provide BRF values in conformity with respective measurements. However, they slightly underestimate the BRF at high zenith angles in the backscattering region where aggregate of 8 columns can simulate the aged snow BRF better.

https://doi.org/10.5194/tc-2020-269
Preprint. Discussion started: 7 October 2020

The Cryosphere Discussions

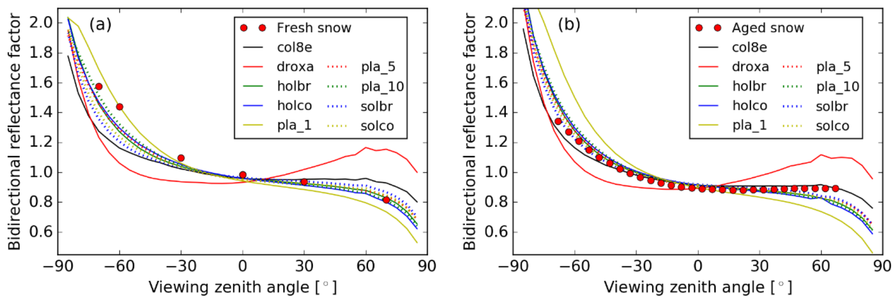

Fig. 4 The comparison of angle dependence of laboratory-measured and simulated snow reflectance: (a) fresh snow sample; (b)aged snow sample. Symbols - measurements, lines – simulations with SCIATRAN assuming different shapes of ice crystals (see legend).

The above analysis demonstrates that the selected database of crystal shapes can be used successfully to reproduce measured BRF of both fresh and aged snow samples. Similar results were obtained by Pohl et al., (2020b). In this paper, top of atmosphere BRF at 865 nm derived from POLarization and Directionality of the Earth's Reflectances 3 (POLDER-3) on Polarization & Anisotropy of Reflectances for Atmospheric Sciences coupled with Observations from a Lidar (PARASOL) measurements over a pure snow surface in Greenland (70.5° N, 47.3° W) on 6 July 2008 were compared with the SCIATRAN simulations, using droxtals, solid bullet rosettes, and solid columns.

According to the above analysis, we can formulate the general algorithm to retrieve SGS and SPS from satellite observations. Satellite provides the wavelength-dependent TOA reflectance, for a given SGS and SPS pair, the minimization between satellite observed TOA reflectance and theoretical simulation is performed. The optimal SGS and SPS are obtained when the difference between observations and simulations reaches the predefined criteria. The SSA is then calculated by the retrieved SGS and SPS.

4 XBAER Algorithm

The retrieval algorithm consists of three stages. The first stage includes the estimation of SGS using the effective Lambertian surface albedo after atmospheric correction for selected

https://doi.org/10.5194/tc-2020-269
Preprint. Discussion started: 7 October 2020

observation geometries and wavelengths. The estimation of SGS is obtained solving the following minimization problem with respect to the effective radius, *r*, of snow crystals:

$$\|\boldsymbol{A}_e - \boldsymbol{R}_s(r)\|^2 \rightarrow \min. \tag{1}$$

Here, $\mathbf{A}_e$ and $\mathbf{R}_s(r)$ are two vectors which components are the effective Lambertian surface albedo and the simulated snow reflectance, respectively. The dimension of these vectors is the number of wavelengths times the number of viewing directions.

The simulation of snow reflectance (components of vectors $\mathbf{R}_s(r)$) was performed using the radiative transfer package SCIATRAN (Rozanov et al., 2014) as described in Section 3. The optical properties of nine ice crystal shapes, listed in Table 1, were used for radiative transfer calculations.

The minimization problem formulated by Eq. (1) was solved separately for each crystal shape using Brent's method (Brent, 1973). The solution of the minimization problem for each crystal habit is characterized by the following residual:

$$\Delta_i = \|A_e - R_s(r_i^*)\|^2, i = 1, 2, ..., 9, \tag{2}$$

where r_i^* is the solution of minimization problem given by Eq. (1) for i^{th} shape of the ice crystal particle.

The second stage is the selection of such *i* (crystal shape) for which Δ_i is minimal. This completes the retrieval process and enables the optimal SGS and SPS to be obtained.

The third stage is to calculate SSA for the retrieved SGS and SPS. To this end, let us rewrite the SSA introduced above in the following equivalent form: SSA = $3/\rho r \cdot (A_t/4A_p)$, where *r* is the effective radius. According to Cauchy's surface area formula (Cauchy, 1841; Tsukerman and Veomett, 2016), the average area of the projections of a convex body is equal to the surface area of the body, up to a multiplicative constant. In our case, this results in $A_t = 4A_p$ and SSA for convex particles such as droxtals, solid columns, and plates are

https://doi.org/10.5194/tc-2020-269
Preprint. Discussion started: 7 October 2020

The Cryosphere Discussions

equal to 3/ρr. In the case of non-convex particles, the calculation of SSA requires the information about total area A_t. Although the database given by Yang et al. (2013) does not contain information about A_t, the total area of non-convex particles can be calculated employing geometric parameters of ice crystal habits presented in Table 1 of Yang et al. (2013). The details of such calculations for non-convex ice crystal habits are given in the Appendix.

The relationship between SSA and SGS for different SPS is presented in Fig. 5. According to Fig. 5, an almost inverse linear relationship between SSA and SGS can be found. The lines, representing droxtal, plate, and column, are overlapped, indicating the same SSA for convex particles. For other SPSs with the same SGS, SSA is larger compared to convex faceted particles. For example, for SGS=100μm, the SSA is 32.7 m^2/kg for convex faceted particles, whereas SSAs for aggregate of 8 columns, hollow bullet rosettes, hollow column, aggregate of 5 plates, aggregate of 10 plates, and solid bullet rosettes are 44.2, 43.4, 37.7, 74.4, 66.8 and 35.6 m^2/kg, respectively. The relative differences range from 9%-128%, depending on the SPS. Taking into account the definition of SSA, one can derive the following relationship between SSA convex and non-convex particles: $SSA_{nc} = SSA_c \cdot (A_t/4A_p)$, where subscript c and nc denotes convex and non-convex particle, respectively. The obtained results reveal that for all non-convex ice crystals under consideration $A_t/4A_p > 1$ and the ratio $A_t/4A_p$ weakly depends on the SGS.

https://doi.org/10.5194/tc-2020-269
Preprint. Discussion started: 7 October 2020

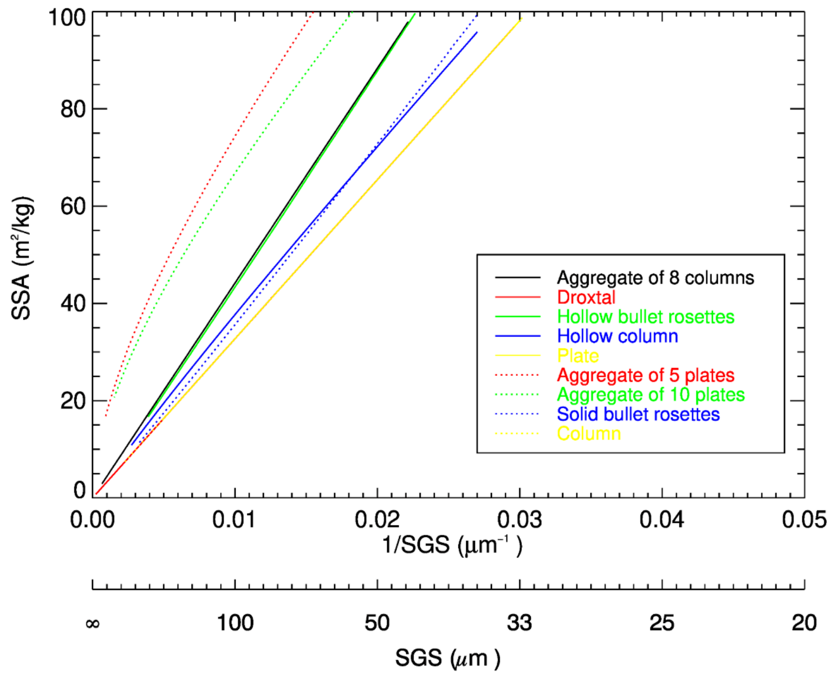

Fig 5. Relationship between snow grain size and specific surface area for different snow particle shape. For a better illustration, the realistic range of specific surface area is limited to 100 m^2/kg.

5 Impact of model parameters uncertainty

The accuracy of any retrieval algorithm depends not only on measurement errors but also on the uncertainty of parameters which cannot be retrieved. In our case, such parameters are ice crystal roughness, aerosol, and cloud contamination. The impacts of these factors on XBAER-derived SGS and SPS have been investigated and will be discussed in this section. The TOA reflectances at selected channels (0.55 and 1.6 µm) and observation directions for SZA, VZA, and RAA of 70°, 30°, and 135° for nadir 70°, 55°, and 135° for oblique, respectively, were calculated using radiative transfer model SCIATRAN. The details of each scenario will be presented in the corresponding sub-section below.

https://doi.org/10.5194/tc-2020-269
Preprint. Discussion started: 7 October 2020

5.1 Impact of ice crystal shape

Since the first stage of the XBAER algorithm is to estimate the SGS assuming a given SPS, it is reasonable to investigate the impact of SPS on the retrieval of SGS. The TOA reflectances of a snow layer at 0.55 and 1.6 µm with above-given observation geometries were calculated using the following settings for snow layer and atmospheric parameters:

- **Snow Layer:** consists of ice crystals with SPS set to be severely roughened aggregate of 8 columns and maximal dimensions [100, 300, 500, 700, 1000, 2000, 3000, 5000] µm, which corresponds to SGS [15, 45.1, 75.2, 105.3, 150.4, 300.8, 451.3, 752.1] µm.
- **Atmosphere:** excluded

The simulated snow reflectances were used as components of vector $\mathbf{A_e}$ in Eq (1). Nine ice crystal shapes from database presented in Yang et al. (2013) are used sequentially in the retrieval process. The atmospheric correction is not performed because the atmosphere is excluded in the forward simulations. This enables avoiding additional errors caused by the atmospheric correction and estimates the pure effect of SPS on the retrieval results. Fig.6 shows the impact of the ice crystal shape on SGS retrieval. Different colors and line styles indicate different ice crystals used in the retrieval process. The black solid line represents the retrieved SGS assuming SPS in the retrieval process is the same as in forward simulations. This line agrees well with the 1:1 line, indicating that the retrieval algorithm has been implemented technically correct. According to Fig.6, one can see both underestimation and overestimation of SGS depending on the ice crystal shape used in retrieval. However, in most cases, an incorrect SPS leads to an underestimation of SGS. In particular, the maximal effect can be seen when ice crystals of plate shape, rather than the correct aggregate of 8 columns, is used (yellow solid line). This result can be easily explained coming back to the right panel of Fig. 2. Indeed, one can see that the same reflectance of the snow layer can be obtained using the plate shape, instead of an aggregate of 8 columns, with significantly smaller SGS. These results reveal that the SPS is an important parameter affecting the accuracy of retrieved SGS.

https://doi.org/10.5194/tc-2020-269
Preprint. Discussion started: 7 October 2020

The Cryosphere Discussions
Open Access
EGU

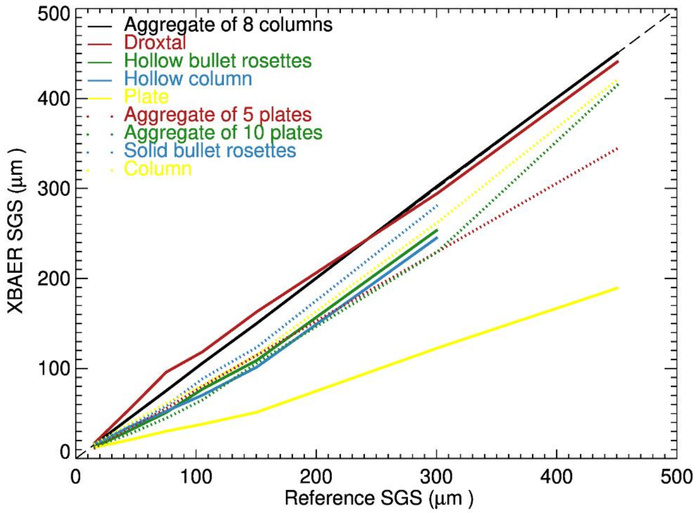

Fig 6. Impact of ice crystal shapes on the retrieval of SGS.

5.2 Impact of SGS/SPS on SSA

Since the SSA is obtained from the retrieved SGS and SPS, an understanding of how the error of SGS and/or SPS propagates to the SSA will provide helpful information to understand the retrieved SSA. Fig. 7 shows the impact of SGS (left) and SPS (right) on XBAER retrieved SSA. The relative error of SGS, $\varepsilon_r = (r - r')/r$, is propagated to the relative error of SSA as $\varepsilon_{SSA} = 1 - 1/(1 - \varepsilon_r)$, and it is independent of reference SSA. The left panel of Fig. 7 depicts ε_{SSA} corresponding to ± 0.16 of ε_r. One can see that this results in 19% and -13.8% of SSA relative errors, which are presented as the upper and lower error boundaries in the left panel of Fig. 7. The systematical error of ±16% for SGS was obtained as the maximal relative difference between XBAER retrieved SGS and both *in-situ* and aircraft measured SGS (as presented in the companion paper). This represents the worst case of SGS error propagation into SSA.

The impact of SPS on SSA is demonstrated in the right panel of Fig. 7. As a reference shape, we have selected in this case the plate, which provides the same SSA as other convex particles. One can see that the SSA of non-convex particles overestimates the SSA of convex particles, which is in line with the results presented in Section 4. For instance, for the same

https://doi.org/10.5194/tc-2020-269
Preprint. Discussion started: 7 October 2020

SGS, the SSA for aggregate 8 columns (non-convex particle) is about 3 times larger than that for doxtal (convex particle). Since the assumption of the sphere (convex particle) is used to measure SSA in-field measures (Gallet et al., 2009; Personal communication with Dr. Nick Rutter), such as observations from SnowEx, the retrieval results of SSA from XBAER will be systematically larger than field measurements in the case of non-convex particles even if the retrieved and measured SGS are similar.

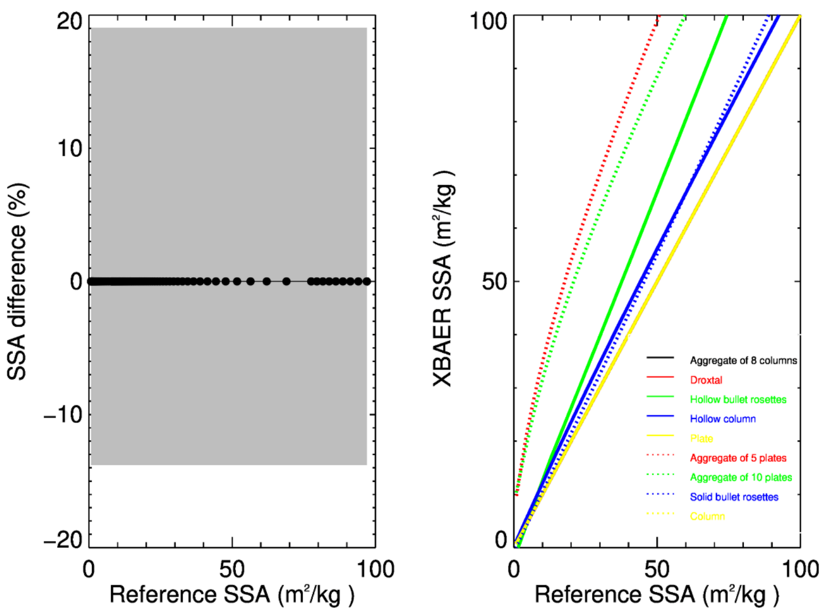

Fig 7. Impact of SGS and SPS on the retrieval of SSA. Left panel (SGS errors): the black line with dots indicate the 0 difference for accurate SGS for aggregate 8 column, the grey area indicate the relative error of SSA introduced by 16% error of SGS; Right panel (SPS selection): different color/line styles indicate different SPS used in the calculation of SSA while the true SPS is set to be „ plate“ or other convex particles.

https://doi.org/10.5194/tc-2020-269
Preprint. Discussion started: 7 October 2020

5.3 Impact of ice crystals surface roughness

The Ice Crystal Surface Roughness (ICSR), indicating ice crystal surface texture, may be important for the retrieval of snow properties from optical sensors such as SLSTR. The ICSR has been used as a new variable in model simulation (Järvinen et al., 2018). Retrieval algorithms of ice cloud parameters frequently based on the assumption that the ice crystal surface is smooth (Kokhanovsky et al., 2019). This assumption can yet introduce large uncertainty in the ice cloud retrieval parameters and, as a consequence, lead to misunderstanding the impacts of ice cloud on global climate change (Järvinen et al., 2018). However, this issue has not yet been discussed for snow. In general, ice crystal surfaces are rougher in clouds than in snow layers due to metamorphism processes (Colbeck, 1980, 1983; Ulanowski et al., 2014). The investigation of the impact of ICSR on retrieval of snow properties provides valuable information to understand the XBAER algorithm. The ICSR according to Yang et al., (2013) is defined similarly as suggested by Cox and Munk (1954) for the roughness of the sea surface. A parameter σ describes the degree of ICSR. The σ values 0, 0.03, and 0.5 are for three surface roughness conditions: smooth, moderate roughness, and severe roughness. The snow layer reflectances were used as components of the vector $\mathbf{A}_e$ in Eq. (1) in the same way as in Section 5.1.

Fig. 8 shows the impact of ICRS on the retrieved SGS, SPS, and SSA. The impact of ICRS on SGS and SSA are relatively small for SGS smaller than ~300 μm. Ignoring the impact of roughness leads, in general, to a slight overestimation on SGS and an underestimation of SSA. The absolute errors of SGS and SSA introduced by ICRS range from 0.3% - 3%, depending on SGS. Due to the inverse almost linear relationship between SSA and SGS, as presented in Fig. 5, for the same SPS, an overestimation of SGS leads to an underestimation of SSA. The slight overestimation can be found if less ICRS is taken into account in retrieval because the snow reflectance with the same SGS and SPS for ICRS = 0.5 is larger than for ICRS = 0.03 due to lower asymmetry factor of ice crystal with more roughened surface roughness, thus the same surface reflectance observed by satellite requires larger SGS for the case with ICRS = 0.03 used in retrieval in contrast to ICRS = 0.5 used in the forward simulation. However, as can be seen from the right panel of Fig.8, the XBAER algorithm still retrieves the correct SPS ignoring the impact of roughness.

https://doi.org/10.5194/tc-2020-269
Preprint. Discussion started: 7 October 2020

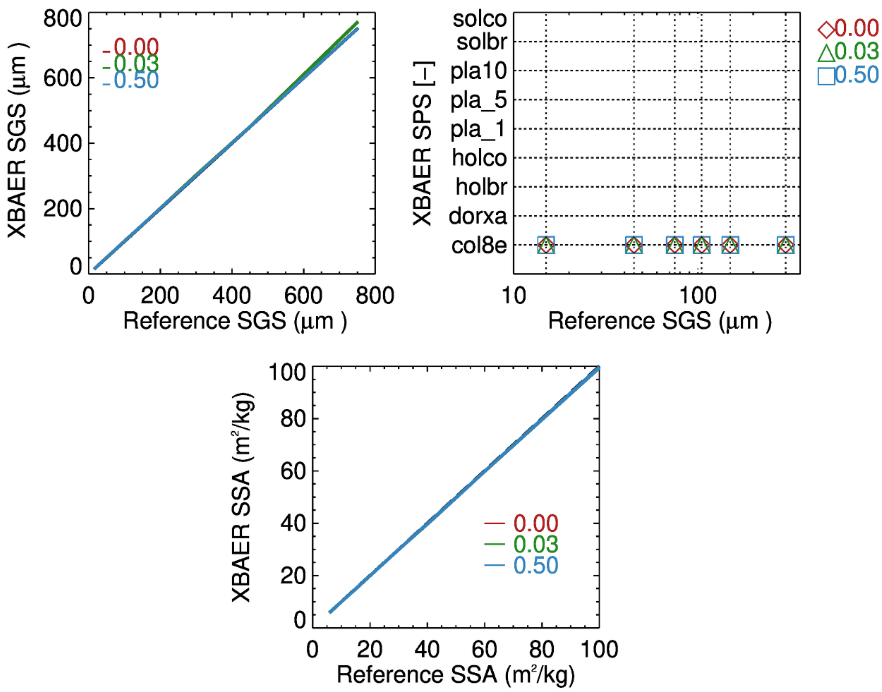

Fig 8. Impact of Ice Crystal Surface Roughness (ICSR) on the retrieval of SGS (upper left) SPS (upper right) and SSA (lower). Different colors indicate different ICSR used in the retrieval.

5.4 Impact of aerosol contamination

The impact of aerosol on the retrieval of snow properties using passive remote sensing can be important because there is limited aerosol information over the cryosphere (Mei et al., 2013a; Mei et al., 2013b; Mei et al., 2020a; Tomis et al., 2015) to perform an accurate atmospheric correction. The use of MERRA simulated AOT, although with good data quality, will still introduce potential aerosol contamination in the XBAER-derived snow properties. The impact of aerosol on snow properties retrieval is much smaller over Arctic regions compared to middle-low latitude due to large absolute uncertainty in the MERRA simulated aerosol over middle-low latitude in wintertime. In order to have a better understanding of aerosol contamination on

https://doi.org/10.5194/tc-2020-269
Preprint. Discussion started: 7 October 2020

The Cryosphere Discussions
Open Access
EGU

snow properties retrieval, the TOA reflectances were calculated at 0.55 and 1.6 μm with above-given observation geometries using the following settings:

- **Snow Layer:** Same as in section 5.1;
- **Atmosphere:**
- Aerosol type is set to be weakly absorbing (Mei et al., 2020b) with AOTs [0.05, 0.08,0.11]. Other atmospheric parameters are set according to Bremen 2D Chemical transport model (B2D CTM) for April at 75° N (Sinnhuber et al., 2009). It is worth to notice this three AOT values represent background, average, and pollution conditions in the Arctic as suggested by Mei et al (2020a; 2020b).

Fig.9 shows the impact of aerosol contamination on the SGS (upper left), SPS (upper right), and SSA (lower) retrieval. These results are obtained by introducing 50% error in AOT at the step of atmospheric correction and can be considered as the worst case for impact of aerosol contamination on retrieved SGS, SPS, and SSA. The surface reflectances estimated after employing the atmospheric correction were used as components of the vector $\mathbf{A}_e$ in Eq. (1). One can see that aerosol introduces systematic underestimation of retrieved SGS for the given scenarios and the magnitude of underestimation increase with the increase of AOT. For a typical background Arctic aerosol condition, with AOT=0.05, aerosol contamination introduces errors in SGS of less than 3% for SGS $\leqslant$150 μm, and less than 7% for 150$\leqslant$SGS<300 μm. The maximal errors introduced by the aerosol contamination increase to 30% and 37% in the case of average and pollution conditions for AOT=0.08 and 0.11, respectively. Please be noted that the AOT values in the Arctic can be even smaller than 0.05, for instance, AOT over Greenland. Thus, the analysis with respect to aerosol contamination is the worst case for a typical Arctic condition.

For the case of AOT = 0.05, SPSs have been correctly retrieved for all SGS values, indicating that under a typical Arctic clean condition, the impact of aerosol is not so large to disturb SPS retrieval. In order to demonstrate the two stages retrieval process and illustrate the impact of aerosol, let us focus on Fig. 10. To facilitate the presentation, we consider the measurement of reflectance at 1.6 μm for a single observation direction (30 °) and at 0.55 μm for the difference of reflectance at two observation angles (30 ° and 55 °). This enables avoiding

https://doi.org/10.5194/tc-2020-269
Preprint. Discussion started: 7 October 2020

The Cryosphere Discussions

the minimization process given by Eq. (1) and represents the retrieval process in the simple graphic form. The left panel of Fig. 10 depicts the determination of an effective radius for each ice crystal form, assuming the correct shape is aggregate of 8 columns with an effective radius 105.4 µm. Solid and dotted lines are surface reflectance of the snow layer consisting of ice crystals with different forms and the dashed line is the measured reflectance after the atmospheric correction. The obtained SGSs are in the range 40 – 120 µm, depending on the selected SPS, and presented in Fig. 10 by solid and dotted vertical lines. In the case of correct crystal shape selection (aggregate of 8 columns) the retrieved SGS is ~110 µm. The right panel of Fig. 10 shows the second stage of the retrieval process, namely, the selection of such crystal shape for which the difference between measured (dashed line) and simulated value (solid black line) is minimal. In the case under consideration the correct shape is selected with an effective radius ~110 µm.

For larger AOT conditions, an inaccurate selection of SPS occurs for all SGS cases, indicating the remaining aerosol information is large enough to decouple the aerosol contribution from the snow surface characteristic. Thus, a quality flag of SPS, associated with AOT, should be introduced in the retrieval of real satellite data. It is interesting to see that "solid bullet rosettes" is the preferable SPS for very strong aerosol contamination cases. This is due to similar scattering properties (shape) of ice crystal and weakly absorbing aerosol, defined in forward simulation. The impact of aerosol contamination, for typical Arctic conditions, introduces less than 5% error in SSA. However, for large aerosol contamination, the around 30% underestimation in SGS linearly introduced about 25% overestimation in SSA, which agrees with the analysis as presented in Fig.7.

https://doi.org/10.5194/tc-2020-269
Preprint. Discussion started: 7 October 2020

The Cryosphere
Discussions
Open Access

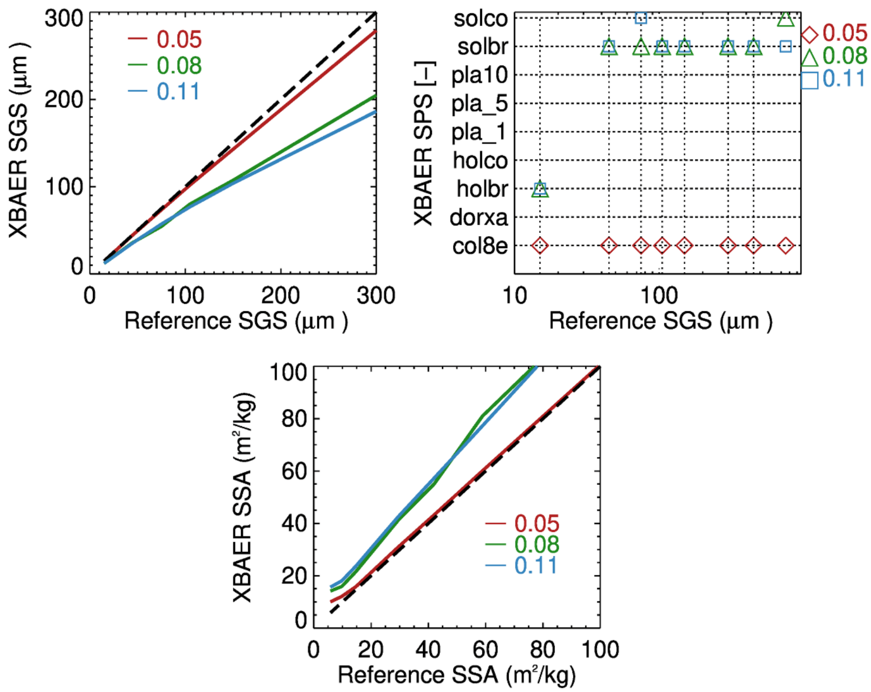

Fig 9. Impact of aerosol contamination on the retrieval of SGS (upper left) SPS (upper right) and SSA (lower). Different colors indicate different AOT used in forward simulations. No atmospheric correction is performed in the retrieval, black dash line is the 1:1 line.

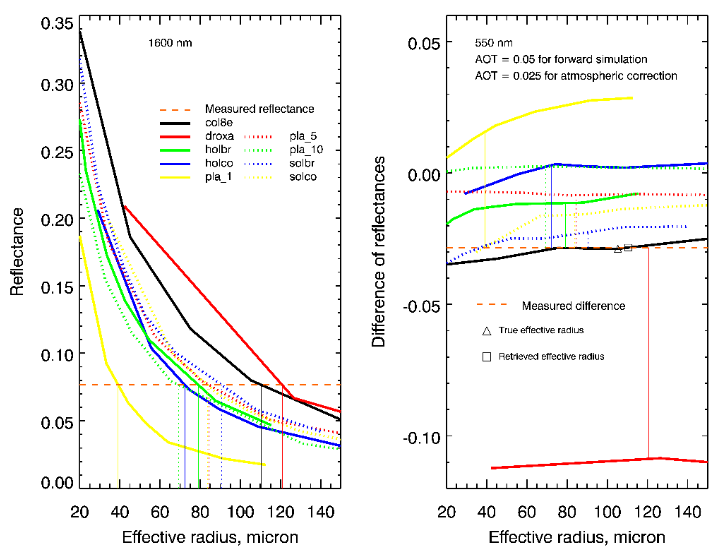

https://doi.org/10.5194/tc-2020-269
Preprint. Discussion started: 7 October 2020

Fig 10 Schematic representation two stages of the retrieval process. Left panel: determination of effective radius for each ice crystal form. Right panel: selection of optimal SGS, SPS pair.

6 Impact of cloud contamination

Any cloud screening method, especially over the cryosphere, may introduce cloud contamination for the retrieval of atmospheric and surface properties (Mei et al., 2017). Understanding of the cloud contamination will provide valuable information to interpret the retrieval results using the SLSTR instrument. To investigate the impact of cloud contamination, the following settings were used to perform the simulations of TOA reflectance:

- **Snow Layer:** Same as section 5.1;
- **Atmosphere:** Aerosol free atmosphere with other parameters as in section 5.4. Additionally, vertically homogeneous ice cloud consisting of aggregate of 8 columns with effective radius of 45 μm and optical thickness [0.1, 0.5, 1.0, 5] is set to be at position of [5 km, 6 km].

Fig. 11 shows the impact of cloud contamination on XBAER retrieved SGS (upper left), SPS (upper right), and SSA (lower). The size of ice crystals in ice clouds is typically smaller than snow grain size (Kikuchi et al., 2013). Our statistical analysis of ice crystal effective radius over Greenland shows an average value in the range of 30-50 μm, which is consistent with previous publications (King et al., 2013; Platnick et al., 2017). According to Fig.11, an overestimation of SGS can be found for SGS less than 45μm (cloud effective radius) and an underestimation of SGS for SGS larger than 45μm. The magnitude of overestimation/underestimation increases with the increase of Cloud Optical Thickness (COT). XBAER derived SGS becomes saturated for COT larger than 0.5. Due to limited photon penetration depth for optically thicker clouds (e.g., COT = 5), the XBAER algorithm retrieves the effective radius of ice crystal in the cloud. This demonstrates that theoretically, the XBAER algorithm can retrieve an ice cloud effective radius without a pre-processing of cloud screening. And this can be further used as post-processing to avoid cloud contamination.

https://doi.org/10.5194/tc-2020-269
Preprint. Discussion started: 7 October 2020

The Cryosphere Discussions
Open Access
EGU

The impact of the cloud on the retrieval of SPS is similar to the impact of aerosol considered above. In short, the cloud plays a larger role for larger SPS (darker TOA) and this impact increases with the increase of COT. However, cloud with large COT can be much easier detected and excluded by the cloud screening algorithm (e.g for the cases with COT > 0.5). SPSs are correctly picked up due to the same SPS used for both the snow layer and the cloud layer. Similar to the impact of aerosol, the underestimation of SGS introduced by the cloud leads to an overestimation of SSA (Fig. 11 (lower panel)). The increase of COT results in saturation of the ice cloud SSA, with a value of 100 m^2/kg in the case of aggregate of 8 columns.

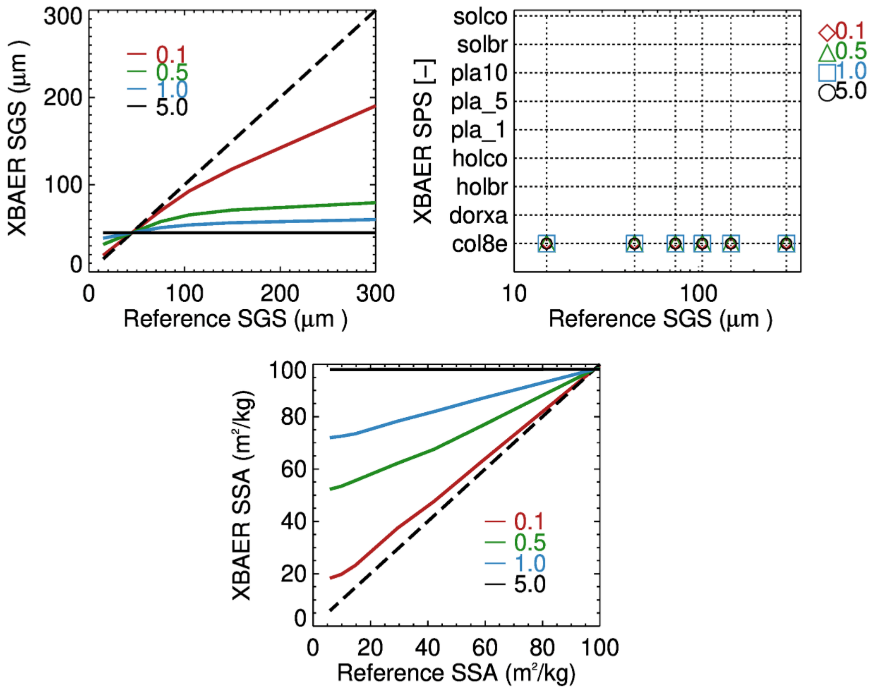

Fig 11. Impact of cloud contamination on the retrieval of SGS (upper left) SPS (upper right) and SSA (lower). Different colors indicate different COTs in forward simulations, black dash line is the 1:1 line.

https://doi.org/10.5194/tc-2020-269
Preprint. Discussion started: 7 October 2020

The Cryosphere Discussions

6 Conclusions

SGS, SPS, and SSA are three important parameters to describe snow properties. They play important roles in the changes in snow albedo/reflectance and impact the atmospheric and energy-exchange processes. A better knowledge of SGS, SPS, and SSA can provide more accurate information to describe the impact of snow on Arctic amplification processes. The information about SGS, SPS, and SSA may also explore new applications to understand the atmospheric conditions (e.g. aerosol loading). Although some previous attempts (e.g. Lyapustin et al., 2009) show the capabilities of using passive remote sensing to derive SGS over a large scale, no publication has been found to derive SGS, SPS, and SSA simultaneously. To our best knowledge, this is the first paper, attempting to retrieve these parameters using satellite observations.

The new algorithm is designed within the framework of the XBAER algorithm. The XBAER algorithm has been applied to derive SGS, SPS, and SSA using the newly launched SLSTR instrument onboard Sentinel-3 satellite. This is the first part of the paper, to describe the algorithm, and to present the sensitivity studies.

The SGS, SPS, and SSA retrieval algorithm is based on the recent publication by Yang et al., (2013), in which a database of optical properties for nine typical ice crystal shapes (aggregate of 8 columns, droxtal, hollow bullet rosettes, hollow column, plate, aggregate of 5 plates, aggregate of 10 plates, solid bullet rosettes, column) are provided. Previous publications show that this database can be used to retrieve ice crystal properties in both ice cloud and snow (e.g., Järvinen et al., 2018; Saito et al., 2019). The algorithm is a LUT-based approach, in which the minimization is achieved by the comparison between atmospherically corrected TOA reflectance at 0.55 and 1.6 μm observed by SLSTR and pre-calculated LUT of surface reflectances under different geometries and snow properties. The retrieval is relatively time-consuming because the minimization has to be performed for each ice crystal shape and the optimal SGS and SPS are selected after 9 minimizations are done. The SSA is then obtained using the retrieved SGS and SPS based on another pre-calculated LUT.

The sensitivity studies with respect to the impacts of ice crystal shape, ICSR, aerosol and cloud contamination on XBAER derived SGS and SPS provide a comprehensive understanding

https://doi.org/10.5194/tc-2020-269
Preprint. Discussion started: 7 October 2020

of the retrieval accuracy of the new algorithm. The main findings of the theoretical considerations are: (1) Ice crystal shape plays an important role for the retrieval accuracy of SGS, the retrieved SGS can differ several times by usage different ice crystal shapes in the retrieval process; (2) Impact of ICSR on the retrieval accuracy of SGS can be neglected, ignoring ICSR completely may introduce maximal 3% error on the retrieval accuracy of SGS, especially for large ice crystals; (3) Assumption of convex particle shape (e.g., sphere) of a non-convex ice crystal leads to the underestimation of the retrieved SSA; (4) The impact of aerosol and cloud increase with the increase of both aerosol/cloud loading and SGS.

Acknowledgements

This research was funded by the Deutsche Forschungsgemeinschaft (DFG, German Research Foundation) – Project-ID 268020496 – TRR 172. The SLSTR data is provided by ESA.

Appendix

According to the definition of specific surface area

$$SSA = \frac{A}{\rho V}, \tag{A1}$$

one needs to calculate the total area A of ice crystal. In the following sections, we consider in details the basic equations to calculate total area and SSA of different ice crystal shapes given in database of Yang et al (2013) and used above within the retrieval algorithm.

- **Droxtal, solid column, plate**

In the case of convex faceted particles such as droxtal, solid column, and plate, the calculation of total area is straightforward and based on the Cauchy's surface area formula:

https://doi.org/10.5194/tc-2020-269
Preprint. Discussion started: 7 October 2020

The Cryosphere Discussions

$$A = 4A_p. \tag{A2}$$

Taking into account that for selected SPS, one can find corresponding V and A_p in database given by Yang et al., (2013), we have the following results for SSA of such particles:

$$SSA = \frac{4A_p}{\rho V}. \tag{A3}$$

➢ **Hollow column**

In this case a solid column includes two equal cavities in the form of a hexagonal pyramid and cannot be considered as convex particle. The aspect ratio of hollow column with the height, d, of hexagonal pyramid is given according to Yang et al., (2013) as:

$$\frac{2a}{L} = \begin{cases} 0.7, & L < 100\mu m \\ \frac{6.96}{\sqrt{L}}, & L \geq 100\mu m \end{cases}, \quad d = 0.25L. \tag{A4}$$

The volume of such hollow column is given by

$$V = V_c - 2V_p, \tag{A5}$$

where the volume of solid column, V_c, and a hexagonal pyramid, V_p, are,

$$V_c = \frac{3\sqrt{3}}{2} a^2 L, \tag{A6}$$

$$V_p = \frac{\sqrt{3}}{2} a^2 d. \tag{A7}$$

Thus, the volume, V, is

$$V = \frac{\sqrt{3}}{2} a^2 (3L - 2d). \tag{A8}$$

Employing the relationship between d and L given by Eq (A4) and excluding a, we have

https://doi.org/10.5194/tc-2020-269
Preprint. Discussion started: 7 October 2020

$$V = \frac{2.5\sqrt{3}}{2} a^2 L \begin{cases} m_0 m_1^2 L^3, & L < 100\mu m \\ m_0 m_2^2 L^2, & L \geq 100\mu m \end{cases}, \tag{A9}$$

where $m = \frac{2.5}{\sqrt{3}/2}$, $m_1 = \frac{0.7}{2}$, and $m = \frac{6.96}{2}$. For a selected volume, V, the length, L, is calculated as follows:

$$L = \begin{cases} [V / m_0 / m_1^2]^{\frac{1}{3}}, & V < V_{100} \\ [V / m_0 / m_2^2]^{\frac{1}{2}}, & V \geq V_{100} \end{cases}, \tag{A10}$$

where $V_{100} = m_0 m_2^2 100^2$.

Let us now calculate the area of each triangle side of the pyramid

$$S_t = \frac{a}{2}\sqrt{d^2 + \frac{3a^2}{4}}. \tag{A11}$$

The area of lateral surface of two pyramids is

$$S_p = 3a\sqrt{4d^2 + 3a^2}. \tag{A12}$$

And the total surface area of hollow column is given by

$$S = 6aL + 3a\sqrt{4d^2 + 3a^2}, \tag{A13}$$

where a and d should be expressed via L according to Eq. (A4).

Having obtained the total area, one can calculate specific surface area

$$SSA = \frac{S}{\rho V}, \tag{A14}$$

➢ **Hollow bullet rosettes**

https://doi.org/10.5194/tc-2020-269
Preprint. Discussion started: 7 October 2020

The Cryosphere Discussions
Open Access
EGU

In this case a solid column includes a cavity in the form of a hexagonal pyramid with height *H* and a hexagonal pyramid with height *t* on the opposite site of column. The aspect ratio and parameters *H* and *t* is given according to Yang et al., (2013) as:

$$\frac{2a}{L} = 2.3104L^{-0.37}, \; t = \frac{\sqrt{3}a}{2\tan(28^{\circ})}, \; H = 0.5(t+L). \tag{A15}$$

The volume of a hollow bullet rosettes is given by

$$V_1 = V_c - V_- + V_+. \tag{A16}$$

Using Eq. (A16), we have

$$V_1 = \frac{3\sqrt{3}}{2}a^2L - \frac{\sqrt{3}}{2}a^2H + \frac{\sqrt{3}}{2}a^2t = \frac{\sqrt{3}}{2}a^2(3L - H + t). \tag{A17}$$

Substituting H as given by Eq (A15), we obtain

$$V_1 = \frac{\sqrt{3}a^2}{4}(5L+t). \tag{A18}$$

Using formula given by Eq (A15), we express parameters *a* and *t* of hollow bullet rosettes via *L*:

$$a = m_a L^{p_a}, \tag{A19}$$

$$t = m_t m_a L^{p_a}, \tag{A20}$$

where coefficients, m_a, m_t, and p_a are

$$m_a = \frac{2.3104}{2}, m_t = \frac{\sqrt{3}}{2\tan(28^{\circ})}, p_a = 1 - 0.37.$$

(A21)

The expression (A18) can be rewritten as:

https://doi.org/10.5194/tc-2020-269
Preprint. Discussion started: 7 October 2020

$$V_1 = \frac{3}{4} m_a^2 L^{2p_a+1} (5 + m_t m_a L^{-0.37}). \quad \text{(A22)}$$

For a desired volume V of hollow bullet rosettes, consisting of 6 equal rosettes (See Table 1), this equation was solved with respect to the length, L, of the hollow bullet rosette using following iterative process:

$$L_n = \left[\frac{2V}{3\sqrt{3} m_a^2 (5 + m_t m_a L_{n-1}^{-0.37})}\right]^{\frac{1}{2p_a+1}}. \quad \text{(A23)}$$

The iterative process starts with L_0=1 and finishes when $\left|\frac{L_n - L_{n-1}}{L_n}\right| \le 10^{-4}$. The total area of hollow bullet rosettes is calculated as;

$$S_1 = 6aL + \frac{3a}{2}\sqrt{4H^2 + 3a^2} + \frac{3a}{2}\sqrt{4t^2 + 3a^2}. \quad \text{(A24)}$$

The SSA is given by

$$SSA = \frac{6S_1}{\rho V}. \quad \text{(A25)}$$

➢ **Solid bullet rosettes**

The aspect ratio and parameter t are given according to Yang et al., (2013) as:

$$\frac{2a}{L} = 2.3104 L^{-0.37}, \; t = \frac{\sqrt{3}a}{2\tan(28^{\circ})}. \quad \text{(A26)}$$

The volume of single solid bullet rosette is

$$V_1 = V_c + V_+. \quad \text{(A27)}$$

Using Eq. (A6), we have

$$V_1 = \frac{3\sqrt{3}}{2} a^2 L + \frac{\sqrt{3}}{2} a^2 t = \frac{\sqrt{3}}{2} a^2 (3L + t). \quad \text{(A28)}$$

https://doi.org/10.5194/tc-2020-269
Preprint. Discussion started: 7 October 2020

Using formula given by Eq (A26), we express parameters *a* and *t* of solid bullet rosette via *L*:

$$a = m_a L^{p_a}, \tag{A29}$$

$$t = m_t m_a L^{p_a}, \tag{A30}$$

Where coefficients, m_a, m_t, and p_a are the same as in the case of hollow bullet rosette given bu Eq. (A21). The expression Eq. (A28) can be rewritten as

$$V_1 = \frac{3}{2} m_a^2 L^{2p_a+1}(3 + m_t m_a L^{-0.37}). \tag{A31}$$

For a desired volume *V* of solid bullet rosettes, consisting of 6 equal rosettes (see Table 1), this equation was solved with respect to the length, *L*, of the solid bullet rosette using following iterative approach:

$$L_n = [\frac{V}{3\sqrt{3}m_a^2(3 + m_t m_a L_{n-1}^{-0.37})}]^{\frac{1}{2p_a+1}}. \tag{A32}$$

The total area of solid bullet rosettes is calculated as;

$$S_1 = 6aL + \frac{3\sqrt{3}a^2}{2} + \frac{3a}{2}\sqrt{4t^2 + 3a^2}. \tag{A33}$$

The SSA is given by

$$SSA = \frac{6S_1}{\rho V}. \tag{A34}$$

➢ **Aggregate of 5 and 10 plates**

According to the paper of Yang et al (2013), Table 1 provides the aspect ratios of the ice crystal habits. In the case of an aggregate of columns or plates, the semi-width *a* and

https://doi.org/10.5194/tc-2020-269
Preprint. Discussion started: 7 October 2020

The Cryosphere Discussions
Open Access
EGU

length L of each hexagonal element of the aggregate are on a relative scale. In order to covert these parameters in absolute values, let us consider the following relationship given in Yang et al (2013) for aspect ratio of plate:

$$\frac{2a}{L}=\begin{cases}1, & a\le 2\mu m\\ m_1 a+m_0, & 2<a<5\mu m\\ ma^p, & a\ge 5\mu m\end{cases} \tag{A35}$$

where constants are: m_1=0.2914, m_0=0.4172, m=0.8038, p=0.526.

Using this expression and accounting for that relative values for a, given in Table 1, are greater than 5μm, we can express L_r via a_r as

$$L_r=\frac{2a_r}{ma_r^p}=\frac{2a_r^{1-p}}{m}. \tag{A36}$$

where subscript r denotes that they are on relative scale. The volume of a hexagonal plate on relative scale is given by

$$v_r=\frac{3\sqrt{3}}{2}a_r^2L_r=\frac{3\sqrt{3}}{m}a_r^{3-p}. \tag{A37}$$

The volume of aggregates of 5 or 10 plates is given by

$$V_r=\frac{3\sqrt{3}}{m}\sum_{i=1}^{N}a_{r,i}^{3-p}, \tag{A38}$$

where N=5 and N=10 for 5 and 10 plates, respectively. The absolute value of the volume, V, for a selected maximal dimension of aggregate of 5 or 10 plates one can find in database presented by Yang et al (2013). Introducing the scaling factor

$$C=\frac{V_r}{V}, \tag{A39}$$

We rewrite expression (A38) as

$$C=\frac{V_r}{C}=\frac{3\sqrt{3}}{mC}\sum_{i=1}^{N}a_{r,i}^{3-p}=\frac{3\sqrt{3}}{m}\sum_{i=1}^{N}a_i^{3-p}, \tag{A40}$$

where the absolute value of semi-width, a_i, is given by

$$a_i=\frac{a_{r,i}}{C^{(3-p)^{-1}}}, \tag{A41}$$

https://doi.org/10.5194/tc-2020-269
Preprint. Discussion started: 7 October 2020

The Cryosphere Discussions
Open Access

Having obtained the absolute value of a_i for each plate, the length L_i is calculated as:

$$L_i = \begin{cases} 2a_i, & a \le 2\mu m \\ \dfrac{2a_i}{m_1 a_i + m_0}, & 2 < a < 5\mu m \\ \dfrac{2}{m_1 a^{(1-p)}}, & a \ge 5\mu m \end{cases} \tag{A42}$$

The total area of a hexagonal plate with semi-width a_i and length L_i is given by

$$S_i = 2\frac{3\sqrt{3}}{2}a_i^2 + 6a_i L_i, \tag{A43}$$

The total area is given by

$$S = \sum_{i=1}^{N} S_i. \tag{A44}$$

Having obtained the total area, one can calculate SSA as the total surface area of a material per unit of mass:

$$SSA = \frac{S}{\rho V}, \tag{A45}$$

where ρ=917 kg/m^3 is the density of ice.

➢ Aggregate of 8 columns

According to M. Saito (private communication), the parameters L and a of the aggregate of 8 columns can be obtained by scaling with respect to the maximum dimension, D. To find these values for different maximal dimensions, we calculate at first the volume of aggregate of 8 columns corresponding to parameters a and L on a relative scale as given in Table 1 of Yang et al (2013).

$$V_r = \frac{3\sqrt{3}}{2}\sum_{i=1}^{8} a_i^2 L_i. \tag{A46}$$

Using the database of Yang et al (2013), one can obtained the maximal dimension, D_r, corresponding to the volume, V_r. Introducing the scaling factor, C_k=D_k/D_r, we have semi-width and length for the aggregate with the maximal dimension D_k:

$$a_{i,k} = a_i C_k, \quad L_{i,k} = L_i C_k. \tag{A47}$$

The total surface of the aggregate on relative scale is given by

$$S_r = 3\sum_{i=1}^{8}(\sqrt{3}a_i^2 + 2a_i L_i). \tag{A48}$$

Accounting for Eq (A47), we have

$$S = C_k^2 S_r. \tag{A49}$$

Having obtained the total area, one can calculate SSA as the total surface area of a material per unit of mass:

$$SSA = \frac{S}{\rho V} = \frac{S_r}{\rho C_k V_r}. \tag{A50}$$

Reference

Aoki, T., Fukabori, M., Hachikubo, A., Tachibana, Y., and Nishio, F.: Effects of snow physical parameters on spectral albedo and bidirectional reflectance of snow surface, *J. Geophys. Res.*, 105(D), 10 219–10 236, 2000.

Baker, I.: Microstructural characterization of snow, firn and ice, *Philosophical Transactions of the Royal Society a-Mathematical Physical and Engineering Sciences*, 377, 10.1098/rsta.2018.0162, 2019.

Battaglia, A., Rustemeier, E., Tokay, A., Blahak, U., and Simmer, C.: PARSIVEL snow observations: a critical assessment, *J. Atmos. Ocean. Tech.*, 27, 333–344, doi:10.1175/2009JTECHA1332.1, 2010.

Baum, B. A., P. Yang, A. J. Heymsfield, C. Schmitt, Y. Xie, A. Bansemer, Y. X. Hu, and Z. Zhang, Improvements to shortwave bulk scattering and absorption models for the remote sensing of ice clouds. *J. Appl. Meteor. Clim*., 50, 1037-1056, 2011

Cauchy, A.: Note sur divers th´eor`ems relatifs `a la rectification des courbes et `a la quadrature des surfaces. C.R. Acad. Sci., 13:1060–1065, 1841.

Colbeck, S. C.: Thermodynamics of snow metamorphism due to variations in curvature, J. Glaciol., 26, 291-301, 10.3189/S0022143000010832, 1980.

Colbeck, S. C.: Theory of metamorphism of dry snow, J. Geophys. Res., 88, 5475-5482, 1983.

Cole, B. H., Yang, P., Baum, B. A., Riedi, J., and C.-Labonnote, L.: Ice particle habit and surface roughness derived from PARASOL polarization measurements, *Atmos. Chem. Phys.*, 14, 3739-3750, https://doi.org/10.5194/acp-14-3739-2014, 2014.

Cox, S. C., and Munk, W. H. : Measurement of the roughness of the sea surface from photographs of the sun's glitter. *J. Opt. Soc. Amer.*, 44, 838–850, 1954.

Dietz, A.J., Kuenzer, C., Gessner, U. and Dech, S. : Remote sensing of snow – a review of available methods, *International Journal of Remote Sensing*, 33:13, 4094-4134, DOI: 10.1080/01431161.2011.640964, 2012.

Domine, F., Gallet, J. C., Barret, M., Houdier, S., Voisin, D., Douglas, T., Blum, J. D., Beine, H., and Anastasio, C.: The specific surface area and chemical composition of diamond dust near Barrow, Alaska, *J. Geophys. Res*., 116, D00R06, 10.1029/2011JD016162 2011.

Domine, F., Picard, G., Morin, S., Barrere, M., Madore, J. B., and Langlois, A.: Major Issues in Simulating Some Arctic Snowpack Properties Using Current Detailed Snow Physics Models: Consequences for the Thermal Regime and Water Budget of Permafrost. *Journal of Advances in Modeling Earth Systems*. 11(1), 34-44, https://doi.org/10.1029/2018MS001445,2019

Donahue, C. , Skiles, S.M. and Hammonds, K.: In situ effective snow grain size mapping using a compact hyperspectral imager. *Journal of Glaciology*, 1–9. https://doi.org/10.1017/jog.2020.68,2020.

https://doi.org/10.5194/tc-2020-269
Preprint. Discussion started: 7 October 2020

The Cryosphere Discussions

Dumont, M., Brissaud, O., Picard, G., Schmitt, B., Gallet, J.-C., and Arnaud, Y.: High-accuracy measurements of snow Bidirectional Reflectance Distribution Function at visible and NIR wavelengths – comparison with modelling results, *Atmos. Chem. Phys*., 10, 2507-2520, https://doi.org/10.5194/acp-10-2507-2010, 2010.

Flanner, M. G. and Zender, C. S.: Linking snowpack microphysics and albedo evolution, *J. Geophys. Res.*, 111, D12208, doi:10.1029/2005JD006834, 2006.

Frei, A., Tedesco, M., Lee, S., Foster, J., Hall, D. K., Kelly, R., and Robinson, D. A.: A review of global satellite-derived snow products, Adv. Space Res., Oceanography, Cryosphere and Freshwater Flux to the Ocean, 50, 1007–1029, 2012.

Gallet, J.-C., Domine, F., Zender, C. S., and Picard, G.: Measurement of the specific surface area of snow using infrared reflectance in an integrating sphere at 1310 and 1550 nm, *The Cryosphere*, 3, 167-182, 2009.

Gardner, A.S. and Sharp, M.J: A review of snow and ice albedo and the development of a new physically based broadband albedo parameterization, *Journal of Geophysical Research*, 115, F01009, doi:10.1029/2009JF001444, 2010Gordon, M. and Taylor, P. A.: The Electric Field During Blowing Snow Events, *Bound-lay. Meteorol.*, 130, 97–115, 2010.

Grenfell, T.C. and Warren, S.G. : Representation of a nonspherical ice particle by a collection of independent spheres for scattering and absorption of radiation. *J. Geophys. Res.* 104 (D24), 31697–31709. http://dx.doi.org/10.1029/1999JD900496,1999

Hagenmuller, P., Matzl, M., Chambon, G., and Schneebeli, M.: Sensitivity of snow density and specific surface area measured by microtomography to different image processing algorithms, *The Cryosphere*, 10, 1039–1054, https://doi.org/10.5194/tc-10-1039-2016, 2016.

Hansen, J. and Nazarenko, L.: Soot climate forcing via snow and ice albedos, *Proc. Nat. Acad. Sci.*, 101, 423–428, 2004

Järvinen, E., Jourdan, O., Neubauer, D., Yao, B., Liu, C., Andreae, M. O., Lohmann, U., Wendisch, M., McFarquhar, G. M., Leisner, T., and Schnaiter, M.: Additional global climate cooling by clouds due to ice crystal complexity, *Atmos. Chem. Phys.*, 18, 15767–15781, https://doi.org/10.5194/acp-18-15767-2018, 2018.

https://doi.org/10.5194/tc-2020-269
Preprint. Discussion started: 7 October 2020

Jiao, Z., A. Ding, A. Kokhanovsky, C. Schaaf, F. Bréon, Y. Dong, Z. Wang, Y. Liu, X. Zhang, S. Yin, L. Cui, L. Mei, Y. Chang: Development of a Snow Kernel to Better Model the Anisotropic Reflectance of Pure Snow into a Kernel-Driven BRDF Model Framework, *Remote Sensing Environment*, 221, 198-209, doi:10.1016/j.rse.2018.11.001, 2019.

Jin, Z., Charlock, T. P., Yang, P., Xie, Y., and Miller, W. : Snow optical properties for different particle shapes with application to snow grain size retrieval and MODIS/CERES radiance comparison over Antarctica. *Remote Sensing of Environment*, 112(9), 3563–3581. doi:10.1016/j.rse.2008.04.011,2008

Kikuchi, K., Kameda, T., Higuchi, K., and Yamashita, A.: A global classification of snow crystals, ice crystals, and solid precipitation based on observations from middle latitudes to polar regions, *Atmos. Res*., 132-133, 460–472, 2013.

King, M.D., Platnick, S., Menzel, W.P., Ackerman, S.A., Hubanks, P.A.: Spatial and temporal distribution of clouds observed by MODIS onboard the Terra and Aqua satellites, *IEEE Trans. Geosci. Remote Sens*. 51 (7), 3826–3852, 2013.

Kokhanovsky, A., Lamare, M.; Danne, O., Brockmann, C., Dumont, M., Picard, G., Arnaud, L., Favier, V., Jourdain, B.; Le Meur, E., Di Mauro, B., Aoki, T., Niwano, M., Rozanov, V., Korkin, S., Kipfstuhl, S., Freitag, J., Hoerhold, M., Zuhr, A., Vladimirova, D., Faber, A.-K., Steen-Larsen, H.C., Wahl, S., Andersen, J.K., Vandecrux, B., van As, D., Mankoff, K.D., Kern, M., Zege, E., Box, J.E.: Retrieval of Snow Properties from the Sentinel-3 Ocean and Land Colour Instrument, *Remote Sens.*, 11, 2280, 2019.

Konig, M., Winther, J.-G. and Isaksson, E.: Measuring snow and glacier ice properties from satelllite, *Reviews of Geophysics*, 39, 1-27, 2001.

Koren, H., Snow grain size from satellite images, SAMBA/31/09, publications.nr.no/5119/Koren_-_Snow_grain_size_from_satellite_images.pdf, 2009 (last acess:7 May, 2018)

Kukla G., Barry, R.G., Hecht, A., Wiesnet, D. eds (1986) SNOW WATCH'85. Proceedings of the workshop held 28-30 October 1985 at the University of Maryland, College Park, MD> Boulder, Colorado, Word Data Center A for Glaciology (Snow and Ice), *Glaciological Data*, Report GD-18, P 215-223, 1986

https://doi.org/10.5194/tc-2020-269
Preprint. Discussion started: 7 October 2020

Langlois, A., Royer, A., Montpetit, B., Roy, A., and Durocher, M.: Presenting Snow Grain Size and Shape Distributions in Northern Canada Using a New Photographic Device Allowing 2D and 3D Representation of Snow Grains. *Frontiers in Earth Science*, 7. doi:10.3389/feart.2019.00347,2020

Legagneux, L. and Domine, F.: A mean field model of the decrease of the specific surface area of dry snow during isothermal metamorphism, J. Geophys. Res., 110, F04011, https://doi.org/10.1029/2004JF000181, 2005.

Legagneux, L., Cabanes, A., and Domine, F.: Measurement of the specific surface area of 176 snow samples using methane adsorption at 77 K, J. Geophys. Res., 107, 4335, 10.1029/2001jd001016, 2002.

Leroux C., and Fily M. : Modeling the effect of sastrugi on snow reflectance, *J. Geophys. Res.*, 103, 25,779-25,788, 1998.

Li, W., Stamnes, K., Chen, B., and Xiong, X.: Snow grain size retrieved from near-infrared radiances at multiple wavelengths, *Geophys. Res. Lett.*, 28, 1699–1702, doi:10.1029/2000GL011641, 2001.

Libois, Q., Picard, G., France, J. L., Arnaud, L., Dumont, M., Carmagnola, C. M., and King, M. D.: Influence of grain shape on light penetration in snow, *The Cryosphere*, 7, 1803–1818, https://doi.org/10.5194/tc-7-1803-2013, 2013.

Liu, J. P., Judith, A. C., Wang, H. J., Song, M. R., and Radley, M. H.: Impact of declining Arctic sea ice on winter snowfall, *P. Natl. Acad. Sci.*, doi:10.1073/pnas.1114910109, 2012.

Livneh, B., Xia, Y., Mitchell, K. E., Ek, M. B., and Lettenmaier, D. P.: Noah LSM snow model diagnostics and enhancements, *J. Hydrometeorol.*, 11, 721–738, 2009.

Lyapustin, A., Tedesco, M., Wang, Y.J., Aoki, T., Hori, M. and Kokhanovsky, A. : Retrieval of snow grain size over Greenland from MODIS, *Remote Sensing of Environment*, 113, 1976-1987,2009.

Mary, A., Dumont, M., Dedieu, J.-P., Durand, Y., Sirguey, P., Milhem, H., Mestre, O., Negi, H. S., Kokhanovsky, A. A., Lafaysse, M., and Morin, S.: Intercomparison of retrieval algorithms for the specific surface area of snow from near-infrared satellite data in mountainous terrain, and comparison with the output of a semi-distributed snowpack model, *The Cryosphere*, 7, 741–761, https://doi.org/10.5194/tc-7-741-2013, 2013.

https://doi.org/10.5194/tc-2020-269
Preprint. Discussion started: 7 October 2020

McFarlane, S. A., Marchand, R. T., and Ackerman, T. P.: Retrieval of cloud phase and crystal habit from Multiangle Imaging Spectroradiometer (MISR) and Moderate Resolution Imaging Spectroradiometer (MODIS) data, *J. Geophys. Res.-Atmos.*, 110, D14201, doi:10.1029/2004JD004831, 2005.

Mei, L.L., Xue, Y., de Leeuw, G., von Hoyningen-Huene, W., Kokhanovsky, A.A., Istomina, L., Guang, J., Burrows, J. P.: Aerosol Optical depth retrieval in the Arctic region using MODIS over snow. *Remote Sensing of Environment*. 128,234 -245, 2013a.

Mei, L.L., Xue, Y., von Hoyningen-Huene, W., Istomina, L., Kokhanovsky, A.A., de Leeuw, G., Guang, J., Burrows, J. P.: Aerosol Optical depth retrieval over snow using AATSR data. *International Journal of Remote Sensing*. 34(14), 5030 – 5041, 2013b.

Mei, L. L., Rozanov, V., Vountas, M., Burrows, J., Levy, R., Lotz, W.: A Cloud masking algorithm for the XBAER aerosol retrieval using MERIS data. *Remote Sensing of Environment*. 197, 141-160, http://dx.doi.org/10.1016/j.rse.2016.11.016, 2017.

Mei, L., Vandenbussche, S., Rozanov, V., Proestakis, E., Amiridis, V., Callewaert, S., Vountas, M., Burrows, J. P., 2020, On the retrieval of aerosol optical depth over cryosphere using passive remote sensing, *Remote Sensing of Enviroment*, 241, 111731, https://doi.org/10.1016/j.rse.2020.111731, 2020a.

Mei, L.L., Rozanov, V., Ritter, C., Heinold, B., Jiao, Z.T., Vountas, M., Burrows, J.P.: Retrieval of aerosol optical thickness in the Arctic snow-covered regions using passive remote sensing: impact of aerosol typing and surface reflection model. *IEEE Transactions on Geoscience and Remote Sensing*. 10.1109/TGRS.2020.2972339, 1-15. 2020b.

Mishchenko MI, Travis LD, Lacis AA. Scattering, absorption, and emission of light by small particles. Cambridge University Press; 2002.

Nakaya, U., Sekido, Y., General classification of snow crystals ad their frequency of occurrence. J. Fac. Sci., Hokkaido Imperial Univ., Ser. II I-9, 234–264, 1938

Nakaya, U.: Snow Crystals: Natural and Artificial, Harvard Univ. Press, Cambridge, 1954.

https://doi.org/10.5194/tc-2020-269
Preprint. Discussion started: 7 October 2020

Painter, T. H., Dozier, J., Roberts, D. A., Davis, R. E., and Greene, R. O.: Retrieval of subpixel snow-covered area and grain size from imaging spectrometer data, *Remote Sens. Environ.*, 85, 64– 77, 2003.

Painter, T.H., Rittger, K., McKenzie, C., Slaughter, P., Davis, R.E., Dozier, J.: Retrieval of subpixel snow covered areas, grain size, and albedo from MODIS, *Remote Sensing of Environment*, 113, 868-879, 2009.

Peltoniemi, J., Hakala, T., Suomalainen, J., & Puttonen, E.: Polarised bidirectional reflectance factor measurements from soil, stones, and snow. *Journal of Quantitative Spectroscopy and Radiative Transfer*, 110(17), 1940-1953,2009

Platnick, S., Meyer, K. G., King, M. D., Wind, G., Amarasinghe, N., Marchant, B., Arnold, G. T., Zhang, Z., Hubanks, P. A., Holz, R. E., Yang, P., Ridgway, W. L., and Riedi, J.: The MODIS Cloud Optical and Microphysical Products: Collection 6 Updates and Examples From Terra and Aqua, *IEEE Trans. Geosci. Remote*, 55, 502–525, 2017

Pirazzini, R., Räisänen, P., Vihma, T., Johansson, M., and Tastula, E.-M.: Measurements and modelling of snow particle size and shortwave infrared albedo over a melting Antarctic ice sheet, *The Cryosphere*, 9, 2357-2381, https://doi.org/10.5194/tc-9-2357-2015, 2015.

Pohl, C., Istomina, L., Tietsche, S., Jäkel, E., Stapf, J., Spreen, G., and Heygster, G.: Broadband albedo of Arctic sea ice from MERIS optical data, The Cryosphere, 14, 165–182, https://doi.org/10.5194/tc-14-165-2020, 2020a.

Pohl C., Rozanov V.V. , Mei L. , Burrows J.P., Heygster G. and Spreen G.: Implementation of an ice crystal single-scattering property database in the radiative transfer model SCIATRAN, J. Quant. Spectrosc. Radiat. Transfer, doi: https://doi.org/10.1016/j.jqsrt.2020.107118,2020b

Pope A., Gareth Rees, W., Fox, A.J. and Fleming, A.: Open access data in polar and cryo spehric remote sensing, *Remote sensing*, 6, 6183-6220, 2014.

Qu, Y., Liang, S.L., Liu, Q., He, T., Liu, S.H. and Li ,X.W.: Mapping surface broadband albedo from satellite observations: A review of literatures on algorithms and products, *Remote sensing*, 7, 990-1020, 2015.

Räisänen, P., Kokhanovsky, A., Guyot, G., Jourdan, O., and Nousiainen, T.: Parameterization of single-scattering properties of snow, *The Cryosphere*, 9, 1277–1301, https://doi.org/10.5194/tc-9-1277-2015, 2015.

https://doi.org/10.5194/tc-2020-269
Preprint. Discussion started: 7 October 2020

Räisänen, P., Makkonen, R., Kirkevåg, A., and Debernard, J. B.: Effects of snow grain shape on climate simulations: sensitivity tests with the Norwegian Earth System Model, *The Cryosphere*, 11, 2919-2942, https://doi.org/10.5194/tc-11-2919-2017, 2017.

Rozanov, V. V., Rozanov, A. V., Kokhanovsky, A. A., and Burrows, J. P.: Radiative transfer through terrestrial atmosphere and ocean: Software package SCIATRAN, *J. Quant. Spect. Rad. Trans.* 133, 13–71, doi:10.5194/acp-8-1963-2008, 2014.

Saito, M., P. Yang, N. G. Loeb, and S. Kato: A novel parameterization of snow albedo based on a two-layer snow model with a mixture of grain habits, *J. Atmos. Sci.*, 76, 1419–1436, 2019.

Satellite Snow Monitoring Community (SSMC), Perspectives for a European Satellite-based Snow Monitoring Strategy, White Paper, *Satellite Snow Monitoring Community*, ESA DUE GlobSnow-2 Consortium, 2014.

Schneider, A., Flanner, M., De Roo, R., and Adolph, A.: Monitoring of snow surface near-infrared bidirectional reflectance factors with added light-absorbing particles, *The Cryosphere*, 13, 1753–1766, https://doi.org/10.5194/tc-13-1753-2019, 2019.

Serreze, M. C. and Francis, J. A.: The Arctic amplification debate, *Climatic Change*, 76, 241–264, 2006.

Sinnhuber, B.-M., Sheode, N., Sinnhuber, M., Chipperfield, M. P., Feng, W.:The contribution of anthropogenic bromine emissions to past stratospheric ozone trends: a modelling study. *Atmos. Chem. Phys.* 9, 2863-2871, https://doi.org/10.5194/acp-9-2863-2009, 2009.

Stamnes, K., Li, W., Eide, H., Aoki, T., Hori,M. and Storvold, R.: ADEOSII/GLI snow/ice products - part I: Scientific basis, *Remote Sens. Environ.*, 111, 258–273, doi:10.1016/j.rse.2007.03.023, 2007.

Taillandier, A. S., Domine, F., Simpson, W. R., Sturm, M., and Douglas, T. A.: Rate of decrease of the specific surface area of dry snow: Isothermal and temperature gradient conditions, J. Geophys. Res., 112, F03003, 10.1029/2006jf000514, 2007.

Tsukerman , E. and Veomett, E. : A Simple Proof of Cauchy's Surface Area Formula, *arXiv*, 1604.05815,2016

Ulanowski, Z., Kaye, P. H., Hirst, E., Greenaway, R. S., Cotton, R. J., Hesse, E., and Collier, C. T.: Incidence of rough and irregular atmospheric ice particles from Small Ice Detector 3 measurements, *Atmos. Chem. Phys.*, 14, 1649-1662, 10.5194/acp-14-1649-2014, 2014.

Tomasi, C., Kokhanovsky, A. A., Lupi, A., Ritter, C., Smirnov, A., O'Neill, N. T., Stone, R. S., Holben, B. N., and Nyeki, S.: Aerosol remote sensing in polar regions, *Earth-Sci. Rev.*, 140, 108–157, doi:10.1016/j.earscirev.2014.11.001, 2015.

Van de Hulst, H :Light Scattering by Small Particles, Dover Publications, 496 pages, 1981

Warren, S. and Wiscombe, W.: A model for the spectral albedo of snow, II: Snow containing atmospheric aerosols, *J. Atmos. Sci.*, 37, 2734–2745, 1980.

Wiebe, H., Heygster, G., Zege, E., Aoki, T., and Hori, M.: Snow grain size retrieval SGSP from optical satellite data: Validation with ground measurements and detection of snow fall events, *Remote Sens. Environ.*, 128, 11–20, https://doi.org/10.1016/j.rse.2012.09.007, 2013.

Xiong, C., & Shi, J.: Snow specific surface area remote sensing retrieval using a microstructure based reflectance model. Remote Sensing of Environment, 204, 838–849. doi:10.1016/j.rse.2017.09.017,2018

Yamaguchi, S., Ishizaka, M., Motoyoshi, H., Nakai, S., Vionnet, V., Aoki, T., Yamashita, K., Hashimoto, A., and Hachikubo, A.: Measurement of specific surface area of fresh solid precipitation particles in heavy snowfall regions of Japan, Cryosphere, 13, 2713-2732, 10.5194/tc-13-2713-2019, 2019.

Yang, P., Bi, L., Baum, B. A., Liou, K.-N., Kattawar, G. W., Mishchenko, M. I. And Cole, B.: Spectrally consistent scattering, absorption, and polarization properties of atmospheric ice crystals at wavelengths from 0.2 to 100 µm, *J. Atmos. Sci.*.70, 330–347, 2013.